SUPPLEMENTARY MATERIAL

Strong coupling of microwave photons to antiferromagnetic fluctuations in an organic magnet

Matthias Mergenthaler,[1,2,*] Junjie Liu,[1] Jennifer J. Le Roy,[1] Natalia Ares,[1] Amber L. Thompson,[3] Lapo Bogani,[1] Fernando Luis,[4] Stephen J. Blundell,[2] Tom Lancaster,[5] Arzhang Ardavan,[2] G. Andrew D. Briggs,[1] Peter J. Leek,[2] and Edward A. Laird[1,†]

[1] *Department of Materials, University of Oxford, Oxford OX1 3PH, United Kingdom*
[2] *Clarendon Laboratory, Department of Physics, University of Oxford, Oxford OX1 3PU, United Kingdom*
[3] *Chemical Crystallography, Chemistry Research Laboratory, University of Oxford, Oxford OX1 3TA, United Kingdom*
[4] *Instituto de Ciencia de Materiales de Aragón (CSIC-U. de Zaragoza), 50009 Zaragoza, Spain*
[5] *Durham University, Centre for Materials Physics, Durham, DH1 3LE, United Kingdom*

(Dated: August 8, 2017)

* matthias.mergenthaler@materials.ox.ac.uk
† edward.laird@materials.ox.ac.uk

I. EXPERIMENTAL SECTION

A. Characterization of the resonator

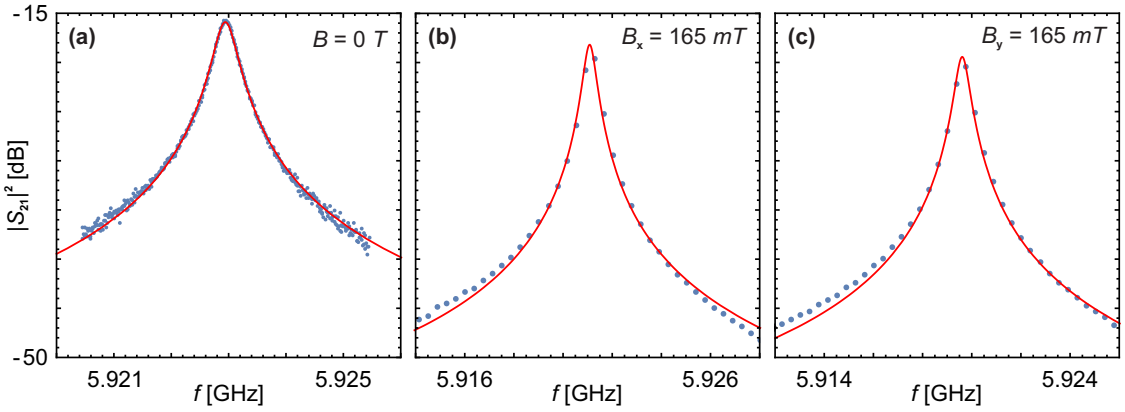

Figure S1. Points: Microwave transmission of the resonator at different magnetic field strengths and orientations. Lines: fits to Eq. (S1), with fit parameters listed in Tab. SI.

To extract the frequency and loaded quality factor Q_L of the resonator after attaching Crystal I, the measured transmission $|S_{21}(\omega)|^2$ was fitted according to

$$|S_{21}(\omega)|^2 = A_0 \frac{\kappa^2}{(\omega - \omega_0)^2 + \kappa^2}, \tag{S1}$$

where the fit parameters are the amplitude A_0, the resonance frequency $\omega_0/2\pi = f_0$ and the linewidth $2\kappa \equiv \omega_0/Q_L$. Figure S2 shows fits at zero magnetic field and in fields of 165 mT applied along x and y. The field was chosen to approach the spin resonance magnetic field, but far enough below it that the hybridization has still no influence on the resonance frequency. Table SI shows the extracted fit parameters.

	B^{ext}	f_0	$\kappa/2\pi$	Q_{L}
-	0 T	5.923 GHz	195 kHz	15200
x	165 mT	5.921 GHz	251 kHz	11800
y	165 mT	5.919 GHz	283 kHz	10500

Table SI. Parameters extracted from Fig. S1

B. Growth and structure of the crystal

All reagents including 2,2-Diphenyl-1-picrylhydrazyl (DPPH; CAS: 1898-66-4), n-hexane, (99+%), and toluene, (99+%), were purchased from Sigma Aldrich or Fisher Scientific and used without further purification. Low temperature X-ray diffraction data were collected from Crystal II using an Oxford Diffraction (Rigaku) SuperNova diffractometer. Data were reduced using CrysAlisPro and solved using SIR92 [S1] within the CRYSTALS suite

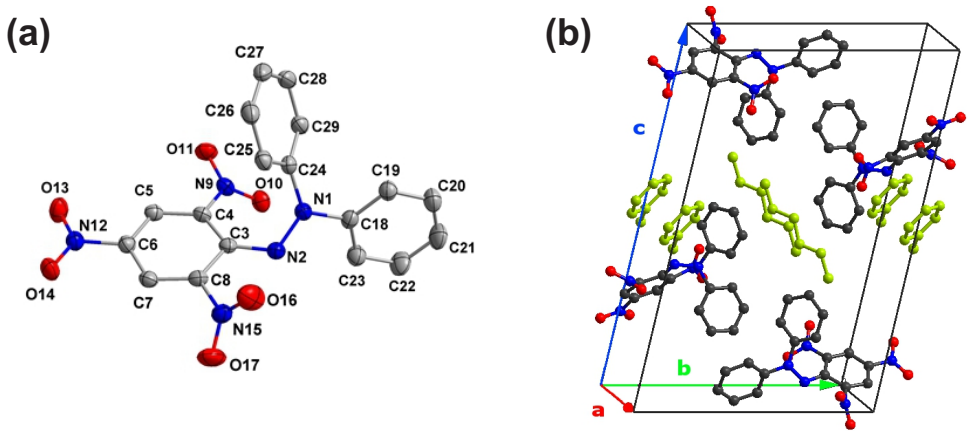

Figure S2. (a) Molecular structure of DPPH with displacement ellipsoids drawn at 50% probability. Color code: carbon (gray), oxygen (red), nitrogen (blue), hydrogen not shown. (b) Unit cell of the measured crystals containing four DPPH molecules, one hexane, and one toluene molecule per cell, with the latter two shown in green. The toluene exhibits crystallographic disorder (not shown). Lattice vectors $\mathbf{a}, \mathbf{b}, \mathbf{c}$ are marked. Lattice constants are $|\mathbf{a}| = 7.4$ Å, $|\mathbf{b}| = 13.5$ Å, $|\mathbf{c}| = 21.7$ Å.

[S2, S3]. The structure was refined using full-matrix least-squares with CRYSTALS to give the unit cell shown in Fig. S2. Disordered solvent in each unit cell was modelled as one toluene molecule. In general, hydrogen atoms were visible in the difference map and refined separately using soft restraints prior to inclusion in the final refinement using a riding model [S4]. There was no evidence of protonation of the central nitrogen atom in each molecule (N2 in Fig. S2). Comparison of the final refinement with that generated using PLATON/SQUEEZE [S5] suggested that the disordered toluene model was a good fit to the electron density. Full refinement details are given in the Supporting Information (CIF file). Crystallographic data (excluding structure factors) have been deposited with the Cambridge Crystallographic Data Centre (CCDC 1475359) and will be available via `http://www.ccdc.cam.ac.uk/data_request/cif`.

C. Bulk susceptibility measurements

1. *High temperature measurements*

Magnetization $M(T)$ was measured as a function of temperature (and converted to susceptibility by the relation $\chi(T) = M(T)/H$) using a Quantum Design MPMS 7 T SQUID. Polycrystalline samples of DPPH were loaded into gelatin capsules, mounted in a plastic drinking straw, and affixed to the end of a stainless steel/brass rod. The sample was cooled from 300 K to 1.8 K.

Results are shown in Fig. S3. Near room temperature the product χT is constant at a value 0.37 emu/K mol Oe, as expected for a paramagnet with $S = 1/2$ and $g = 2.0$ [S6, Eq. (A.8)]. Below ~ 100 K, the susceptibility decreases, consistent with antiferromagnetic spin interactions. The additional structure in the data observed on cooling may reflect different values of the intermolecular exchange along different crystallographic directions, not included in the chain model in the main text.

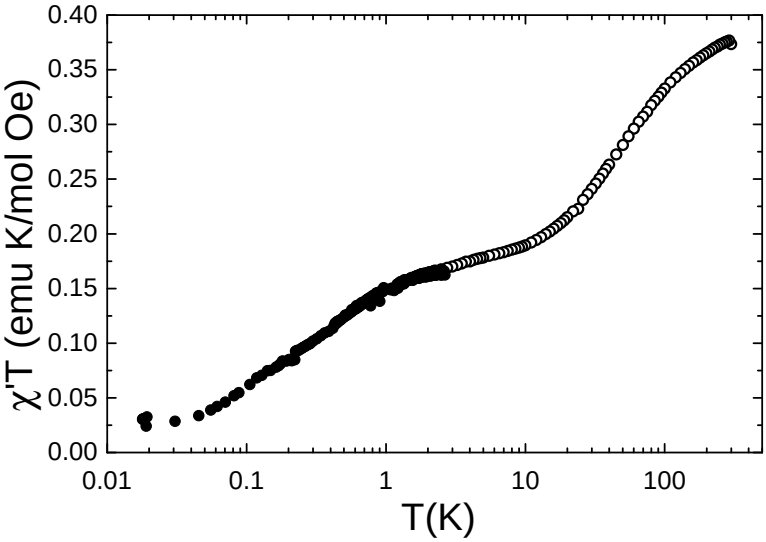

Figure S3. Magnetic susceptibility of a polycrystalline sample of DPPH. Data is plotted as the χT product, which was corrected for the diamagnetic background. High- and low-temperature measurements are marked with open and filled circles respectively.

2. Low temperature measurements

To measure susceptibilty below 1.8 K, we used a 30 μm micro-SQUID susceptometer [S7]. Polycrystalline samples of DPPH were attached with Apiezon N grease to a SQUID loop. The sample was cooled from 3 K to 16 mK in a dilution refrigerator and an AC magnetic field of amplitude 0.25 Oe was applied with its frequency varied from 0.3 Hz to 200 kHz.

Figure S4 shows representative results of the in-phase, χ', and out-of-phase, χ'', component of the susceptibility χ. Below $\sim$ 1.7 K the product $\chi' T$ is decreasing, which is consistent with antiferromagnetic interactions. However, no evidence of a phase transition (in the form of a peak in $\chi'(T)$) could be detected, indicating that any transition from PM to AFM occurs below 16 mK. From the peak in $\chi''(T)$ it is evident that there is an onset of slow relaxation below 150 mK.

D. Muon spin relaxation measurements

To further exclude long-range magnetic ordering we carried out muon-spin relaxation measurements down to T = 19 mK. Measurements were performed at the Swiss Muon Source, Paul Scherrer Institute using the LTF instrument. Roughly 100 mg of polycrystalline DPPH was attached with vacuum grease to a thin silver foil, which in turn was attached to a silver plate mounted on the cold finger of the dilution refrigerator. In a μ^+SR experiment spin polarized muons are implanted into the sample. The measured quantity is the asymmetry $A(t)$, which is proportional to the spin polarization of the muon ensemble.

This asymmetry at each temperature (Fig. S5) shows a broadly Gaussian relaxation, which we attribute to the magnetism of randomly oriented quasistatic nuclear spins. Significantly, the spectra are quite temperature independent up to T = 0.8 K and we do not

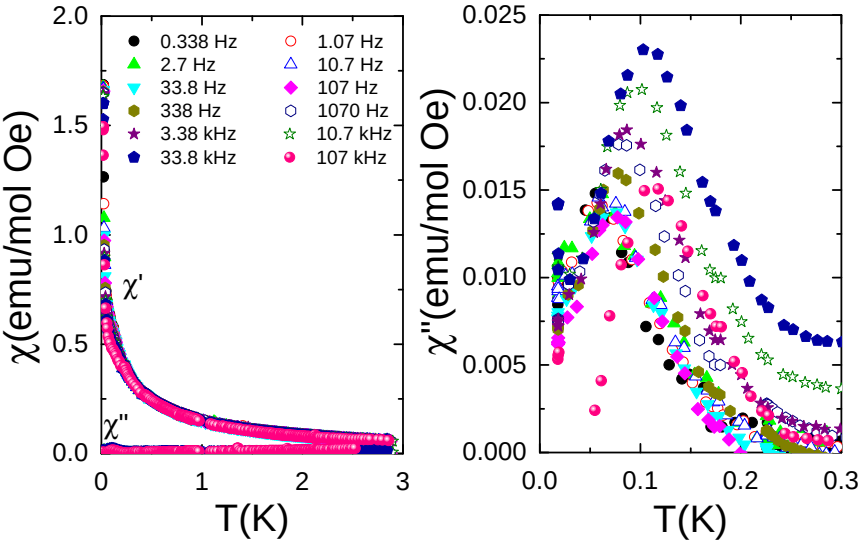

Figure S4. Magnetic susceptibility of a polycrystalline sample of DPPH for $T \leq 3$ K, measured with twelve different ac-magnetic field frequencies. Data is shown for the in-phase, χ', and out-of-phase, χ'', component.

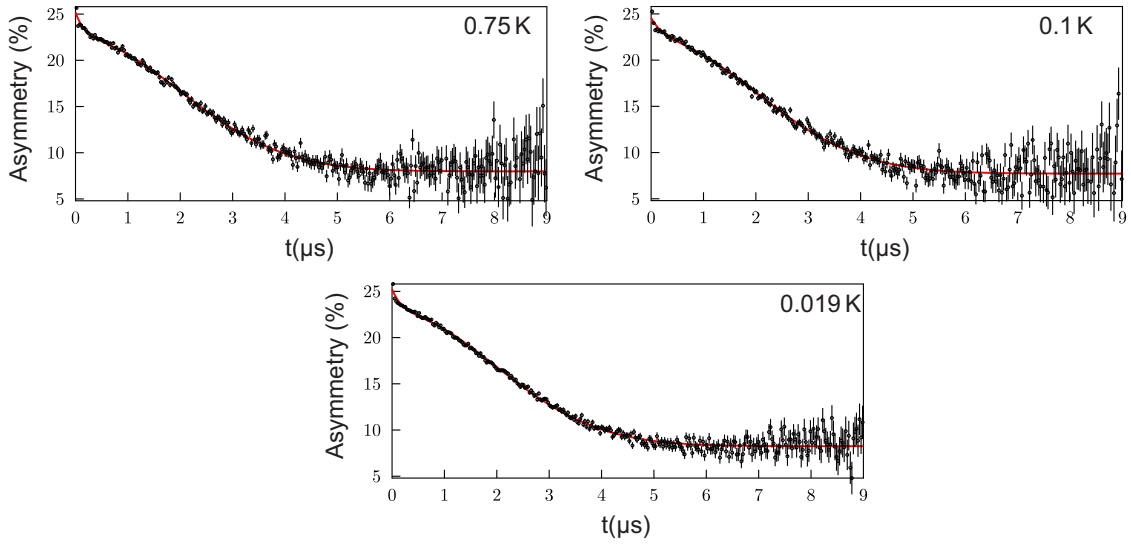

Figure S5. Example asymmetry as a function of time for a polycrystalline sample of DPPH , measured at three temperatures

observe any spontaneous oscillations in the asymmetry or a shift in the baseline that might be expected for a transition to a regime of long range magnetic order. We therefore conclude that the system is magnetically disordered down to $T = 19$ mK, with electronic moments fluctuating outside the muon time window, causing them to be motionally narrowed from the spectra.

E. Measurement of a second crystal

The measurements of Fig. 3(a)-(b) and Fig. 4(a) in the main text were rerun with a second sample (Crystal II) from a different growth batch, which used a newly opened bottle of DPPH powder precursor. The measurements and the extracted parameters are similar to the results presented in the main text. Following these measurements, X-ray characterization was performed on this crystal, confirming the structure of Fig. S2.

Figure S6 shows measurements and fits similar to Fig. 2 of the main text. Extracted parameters are given in Table SII. The magnetic resonance field is slightly lower than in the main text, consistent with the lower cavity frequency (presumably because Crystal II was slightly larger and acted as a dielectric load). Measurements similar to Fig. 3 of the main text are shown in Fig. S6, again with similar results. The extracted anisotropy of B_{MR} and the spin-flip field are the same as in the main text, to within 4 %, confirming reproducibility.

T (K)	Axis	B_{MR} (mT)	$g_{\mathrm{eff}}/2\pi$ (MHz)
4	x	208.36 ± 0.02	17.01 ± 0.1
4	y	209.32 ± 0.02	12.75 ± 0.1
0.015	x	200.6 ± 0.01	38.04 ± 0.1
0.015	y	210.86 ± 0.06	29.59 ± 0.3

Table SII. Resonance parameters extracted from Fig. S6 for different temperatures and magnetic field orientations.

To confirm that the anisotropy is associated with the crystal rather than the resonator we repeat the low-T fundamental-mode measurement of Fig. S7(a) after rotating the crystal by 90° in the xy plane. The data shows the expected shift (Fig. S8(a)), confirming that the anisotropy arises from the crystal structure rather than e.g. screening by the resonator. We also measure the crystal in a configuration rotated by approximately 90° in yz in order to

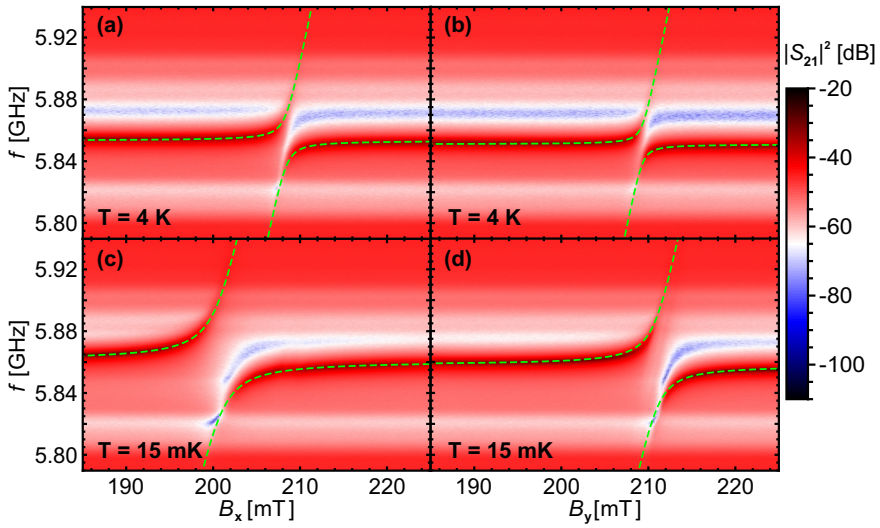

Figure S6. Transmission as a function of external magnetic field $B_{x,y}$ and resonator probe frequency f, measured at two different temperatures using Crystal II. Superimposed on each panel are fits (dashed lines) using Eq. (1) from the main text.

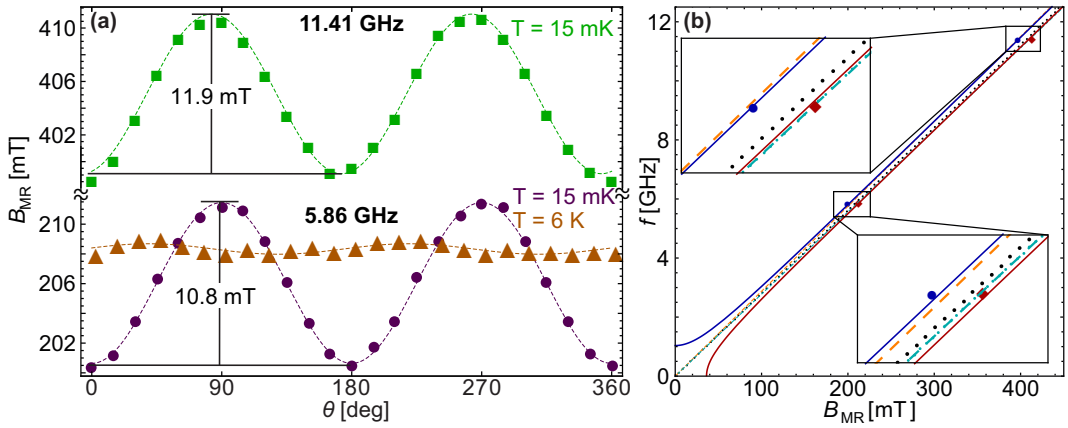

Figure S7. As Fig. 3 of the main text, for measurements on Crystal II. (a) Resonance magnetic field B_{MR} as function of field angle θ at different cavity modes and temperatures, with fits. (b) Plot of the MR frequency as a function of resonance magnetic field, fitted with paramagnetic dispersion relation as in main text (dashed/dotted/dot-dashed lines) and antiferromagnetic dispersion relation (main text Eq. 3, solid lines).

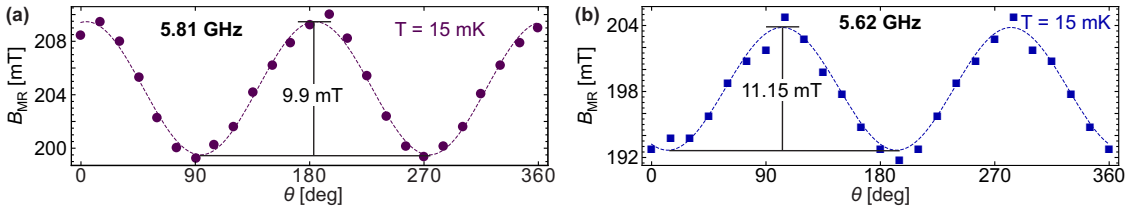

Figure S8. (a) Resonance magnetic field B_{MR} as function of field angle θ, after the crystal has been rotated by 90° in the xy plane. Data is measured near the fundamental mode and at $T = 15$ mK. Compared to Fig. S7 (a) the trace is shifted by 90°, as expected due to the crystal rotation. (b) Equivalent data after rotation by $\sim 90°$ in the yz plane from configuration of Fig. S7.

map the anisotropy axis in three dimensions. The angle dependence in this configuration is shown in Fig. S8(b). Although the anticrossing was harder to identify for some field angles in this configuration, the estimated resonance positions show the same sinusoidal dependence as for Fig. S7(a) and indicate uniaxial behaviour with anisotropy axis along x in Fig. 1 main text.

The temperature dependence of B_{MR} is similar as for Crystal I (Fig. S9). Here the temperature below which the spins in the crystal fail to thermalize is estimated to be around $T \approx 75$ mK. A similar value is also estimated from B_{MR} at the first harmonic (Fig. S9 inset). Performing the same analysis as in Fig. 4 of the main text, we extract for the one-dimensional model similar values $J/k_{\mathrm{B}} = 235$ mK and $J^{\mathrm{A}}/k_{\mathrm{B}} = -7.5$ mK.

II. MODELLING THE TEMPERATURE-DEPENDENT FREQUENCY SHIFT

In this section, we explain the model leading to the fits in Fig. 4 of the main text. We use the spin chain Hamiltonian Eq. (4) of the main text.

Because exchange interaction between spins leads to hybridization of the eigenstates, the

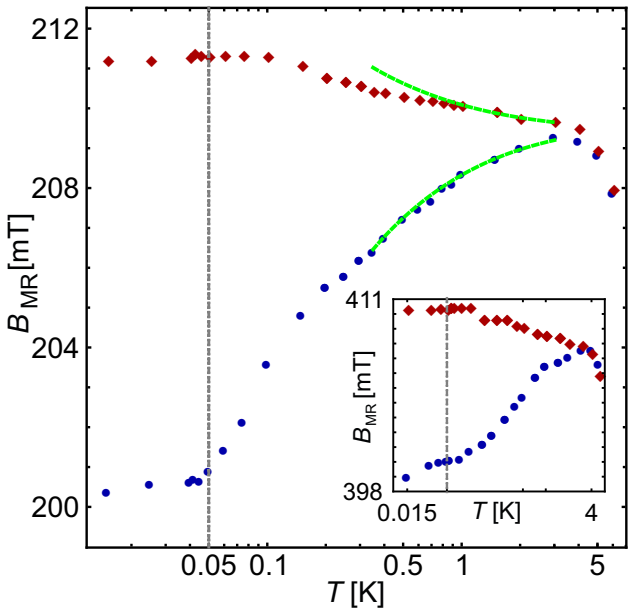

Figure S9. Data and analysis similar to Fig. 4(a) of the main text, for Crystal II. Main panel: temperature dependence of B_{MR} (points) with model (lines) for fundamental mode of the resonator. Inset: same data for first harmonic mode.

magnetic resonance frequency in general shifts away from the paramagnetic value as the crystal is cooled into its antiferromagnetic phase. At high temperature, spin correlations are negligible and the magnetic resonance frequency is given by the single-spin Zeeman splitting. At lower temperatures, as nearby spins become correlated, there is an exchange shift. In the antiferromagnetic phase, the magnetic resonance frequency corresponds to the energy of a long-wavelength magnon.

For this one-dimensional model, the shift calculated in perturbation theory (Eq. (5) of the main text) was evaluated in Ref. [S8]:

$$\delta f_{\parallel} = -4\frac{J^{\mathrm{A}}}{h}\frac{\langle S_i^x S_{i+1}^x - S_i^y S_{i+1}^y\rangle}{\langle S^x\rangle/N} \qquad \text{for } \mathbf{B} \text{ along } x \tag{S2}$$

$$\delta f_{\perp} = \quad 2\frac{J^{\mathrm{A}}}{h}\frac{\langle S_i^y S_{i+1}^y - S_i^x S_{i+1}^x\rangle}{\langle S^y\rangle/N} \qquad \text{for } \mathbf{B} \text{ along } y. \tag{S3}$$

where N is the number of spins in the crystal. Thus, given the anisotropic exchange strength J^{A}, the measured frequency shift is a direct measure of temperature-dependent correlation functions.

Extracting the exchange parameters J and J^{A} from data requires a knowledge of the correlation functions in Eq. (S2-S3). Even in this comparatively simple model, these are not known. However, we can estimate them following Ref. [S8] by making two additional assumptions:

1. We rely on the smallness of $\mathcal{H}'$ compared to $\mathcal{H}^0$ to approximate

$$\langle ... \rangle \approx \langle ... \rangle_0. \tag{S4}$$

In other words, the thermal expectation values in Eqs. (S2-S3), which are determined by the entire Hamiltonian $\mathcal{H}$, can be replaced by thermal expectation values $\langle ... \rangle_0$ under the unperturbed Hamiltonian $\mathcal{H}^0$.

2. We use a classical spin model in which the quantum mechanical spin operators are replaced by classical vectors [S9].

Because of the rotational symmetry of $\mathcal{H}^0$, assumption (1) immediately leads to the equivalence of the two sets of expectation values in Eqs. (S2-S3), implying that the frequency shifts along the two directions should differ by a factor -2. This is in fair agreement with the data of Fig. 4, supporting this model.

Assumption (2) reflects the correspondence of quantum and classical pictures at high temperature. It allows the expectation values to be evaluated by expanding two-spin correlators at finite field in terms of higher-order correlators at zero field [S8]. The result is (to lowest order in J^{A}/J):

$$\delta f_{||} = \frac{2J^{\mathrm{A}} g\mu_{\mathrm{B}} B}{5hJv}\left\{\frac{2+uv}{1-u^2} - \frac{2}{3v}\right\} \tag{S5}$$

$$\delta f_{\perp} = -\frac{\delta f_{||}}{2}, \tag{S6}$$

expressed in terms of dimensionless parameters

$$u(J,T) \equiv \coth w - 1/w \tag{S7}$$

$$v(J,T) \equiv -1/w \tag{S8}$$

$$w \equiv \frac{2JS(S+1)}{k_{\mathrm{B}}T}. \tag{S9}$$

The fit curves in Fig. 4 derived from Eqs. (S5-S6) are then:

$$B_{\mathrm{MR}}(||) = \frac{h(f_0 + \delta f_{||})}{g\mu_{\mathrm{B}}} \tag{S10}$$

$$B_{\mathrm{MR}}(\perp) = \frac{h(f_0 + \delta f_{\perp})}{g\mu_{\mathrm{B}}} \tag{S11}$$

with $g = 2$. The failure of the fits at low temperature presumably reflects the increasing importance of quantum correlations, neglected by assumption (2) above, or of interactions beyond one dimension. Thus, to the extent that our spin-chain approximation is correct, the data of Fig. 4 provide a measurement of the spin correlation function that is more accurate than provided by the calculation relying on assumption (2) above.

III. COLLECTIVE COUPLING PARAMETERS

A. Single spin coupling rate

The single spin-photon coupling rate, g_{s}, is proportional to the vacuum magnetic field B_{vac}, of the resonator [S10]

$$g_{\mathrm{s}} = \frac{g\mu_{\mathrm{B}} B_{\mathrm{vac}}}{4\hbar}, \tag{S12}$$

where $g = 2.0037$ is the Landé g-factor of DPPH, μ_{B} the Bohr magneton, and $\hbar$ the Planck constant. From the resonator's geometry [S10], we approximate

$$B_{\mathrm{vac}} \approx \frac{\mu_0 I_{\mathrm{vac}}}{2(w+2s)}, \tag{S13}$$

where μ_0 is the vacuum magnetic permeability, I_{vac} the zero-point current in the resonator, and w and s the center conductor width and spacing from the lateral groundplanes, respectively. The zero-point current of a resonator with characteristic impedance Z_0 and resonance frequency f_0 is given by [S10]

$$I_{\mathrm{vac}} = \pi f_0 \sqrt{\frac{h}{Z_0}} \tag{S14}$$

For our resonator with $Z_0 = 50\ \Omega$, $f_0 = 5.921$ GHz, $w = 50$ μm and $s = 5.3$ μm this yields $B_{\mathrm{vac}} \approx 7 \times 10^{-10}$ T and therefore $g_{\mathrm{s}}/2\pi \approx 5$ Hz.

B. Number of coupled radicals in crystal

The DPPH crystal was measured to have a length of 365 μm. The effective coupled width of the crystal is assumed to be $w + 2s = 60.6$ μm. Additionally, a penetration depth of the vacuum magnetic field of 4 μm is assumed [S11]. This results in a coupled crystal volume of $V = 1 \times 10^{-7}\ \mathrm{cm}^3$. Taking the density of molecules from the diffraction data (Fig. S2) as $\rho_V \sim 2 \times 10^{21}\ \mathrm{cm}^{-3}$, then the number of coupled radicals in our crystal is $N = \rho_V V \sim 1.7 \times 10^{14}$.

[S1] A. Altomare, G. Cascarano, C. Giacovazzo, A. Guagliardi, M. C. Burla, G. Polidori, and M. Camalli, Journal of Applied Crystallography **27**, 435 (1994).

[S2] P. Parois, R. I. Cooper, and A. L. Thompson, Chemistry Central journal **9**, 30 (2015).

[S3] P. W. Betteridge, J. R. Carruthers, R. I. Cooper, K. Prout, and D. J. Watkin, Journal of Applied Crystallography **36**, 1487 (2003).

[S4] R. I. Cooper, A. L. Thompson, and D. J. Watkin, Journal of Applied Crystallography **43**, 1100 (2010).

[S5] A. L. Spek, Journal of Applied Crystallography **36**, 7 (2003).

[S6] S. Blundell, *Magnetism in Condensed Matter* (Oxford University Press, 2001).

[S7] E. Bellido, P. González-Monje, A. Repollés, M. Jenkins, J. Sesé, D. Drung, T. Schurig, K. Awaga, F. Luis, and D. Ruiz-Molina, Nanoscale **5**, 12565 (2013).

[S8] K. Nagata and Y. Tazuke, Journal of the Physical Society of Japan **32**, 337 (1972).

[S9] M. E. Fisher, American Journal of Physics **32**, 343 (1964).

[S10] G. Tosi, F. A. Mohiyaddin, H. Huebl, and A. Morello, AIP Advances **4**, 087122 (2014).

[S11] M. Jenkins, T. Hümmer, M. José Martínez-Pérez, J. García-Ripoll, D. Zueco, and F. Luis, New Journal of Physics **15**, 95007 (2013).